J. Fluid Mech. (1971), *vol.* 47, *part* 2, *pp.* 353–379
Printed in Great Britain

Dynamical evolution of two-dimensional unstable shear flows

By N. J. ZABUSKY AND G. S. DEEM
Bell Telephone Laboratories, Whippany, N.J. 07981

(Received 23 April 1970 and in revised form 19 October 1970)

A direct numerical integration of the time-dependent, incompressible Navier–Stokes equations is used to treat the nonlinear evolution of perturbed, linearly unstable, nearly parallel shear flow profiles in two dimensions. Calculations have been made for infinite (inviscid) and finite Reynolds numbers. The latter results are compared with laboratory measurements of Sato & Kuriki for wakes behind thin flat plates, and many of the detailed features are in excellent agreement, including mean flow profiles with 'overshoot' development, first harmonic energy profiles with off-axis nulls, and first harmonic phase profiles. The linear instability saturates by forming a vortex street consisting of elliptical vortex pairs. The solutions are followed for times up to eleven linear exponentiation times of the unstable disturbance. A *new* low-frequency non-linear oscillation is found, which explains the features of the above experiment, including the nearly periodic phase inversions in the first harmonic component of the longitudinal velocity. It results from a nutation of the elliptical vortices with respect to the mean flow direction. Inertial range spectral energy properties are also examined. Inviscid solutions have large wave-number spectral energies obeying the approximate power law, $E_k \sim k^{-\mu}$, where μ lies between 3 and 4.

1. Introduction

In recent years, analysts have spent much effort attempting to understand the development of unstable two-dimensional flows described by the Navier–Stokes equations. Sato & Kuriki (1961) and Mattingly (1968) have performed laboratory experiments which characterize the development of unstable two-dimensional wakes. There is still a large gap between *approximate* analytical solutions of the equations and laboratory measurements, because of the usual difficulties in solving nonlinear dynamical problems.

In this paper we describe numerical finite-difference solutions of the two-dimensional incompressible Navier–Stokes equations (initial-boundary-value problems). These solutions help to close the analytical/experimental gap. We present results which have many features of the Sato–Kuriki wake experiment, including development of a double row of elliptical vortices, mean flow evolution including back-flow, and first harmonic 'cross-stream' amplitude and phase development. Sufficient information is presented to aid analysts in evaluating their simplifying assumptions, and to provide guidance for future analytical directions.

For example, in the case of a Gaussian wake-profile excited by one mode, after more than 11 exponentiation times the most unstable linear mode does *not* become stationary in time, as suggested by Landau (Landau 1944; Landau & Lifschitz 1959, p. 104). Instead, a long-time, nearly periodic behaviour develops, and is associated with the 'nutation' of vortices with respect to the mean flow. This new phenomenon, and the nutation frequency, correlate with experimentally observed characteristics of two-dimensional wakes.

These computational results are being studied in an analytic/computational/experimental/*synergetic* (Zabusky 1966, p. 223) working mode. This ACES approach provides us with a deeper insight into the nonlinear dynamical processes involved.

2. Difference equations, boundary and initial conditions

2.1 *Difference equations*

We solve the time-dependent, incompressible Navier–Stokes equations,

$$\partial_t \mathbf{u} + \nabla . (\mathbf{u} \circ \mathbf{u}) = -\nabla p + \nu \nabla^2 \mathbf{u}, \tag{2.1}$$

$$\nabla . \mathbf{u} = 0, \tag{2.2}$$

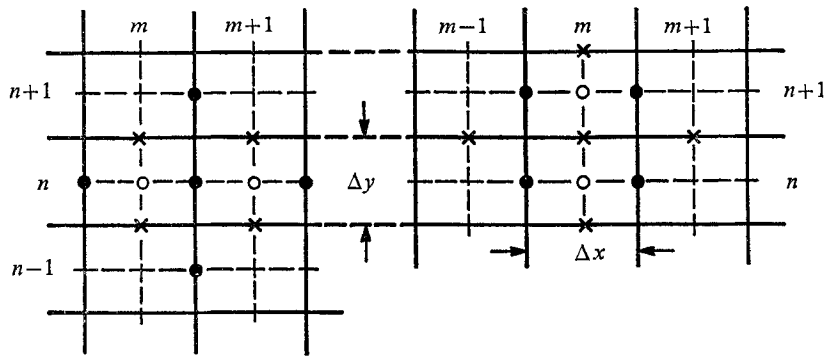

FIGURE 1. Lattice points used in the computation of $u_{m+\frac{1}{2},n}$ and $v_{m,n+\frac{1}{2}}$. ●, u; ×, v; ○, p.

where, in two dimensions,

$$\mathbf{u} = [u(x, y, t), v(x, y, t)], \tag{2.3}$$

and

$$\nabla = (\partial_x, \partial_y). \tag{2.4}$$

The operation ∘ is a dyadic tensor product, and ν is the constant viscosity.

We use a staggered spatial lattice of mesh points (Welch *et al.* 1966), indicated in figure 1. $u_{m+\frac{1}{2},n}$ and $v_{m,n+\frac{1}{2}}$ denote values of the velocity components defined, respectively, on the x and y lattice cell boundaries. $p_{m,n}$ denotes the pressure at the centre of cell (m, n). Values of the velocities at cell centres (or corners) are defined as averages, e.g.

$$\left.\begin{aligned} u_{m,n} &= \tfrac{1}{2}(u_{m-\frac{1}{2},n} + u_{m+\frac{1}{2},n}), \\ u_{m+\frac{1}{2},n+\frac{1}{2}} &= \tfrac{1}{2}(u_{m+\frac{1}{2},n+1} + u_{m+\frac{1}{2},n}). \end{aligned}\right\} \tag{2.5}$$

δ_x and δ_y denote one-sided difference operators

$$\delta_x p_{m,n} = (p_{m+1,n} - p_{m,n})/\Delta x, \tag{2.6}$$

where Δx and Δy are the constant lattice spacings in the x and y directions. Keeping time continuous for the moment, we replace the x component of (2.1), centred at $(m+\frac{1}{2}, n)$, by

$$\partial_t u_{m+\frac{1}{2},n} + \delta_x(u^2_{m,n}) + \delta_y(u_{m+\frac{1}{2},n-\frac{1}{2}} v_{m+\frac{1}{2},n-\frac{1}{2}}) = -\delta_x p_{m,n} + \nu\delta_x(\delta_x u_{m-\frac{1}{2},n}). \tag{2.7}$$

We treat the y component of (2.1), centred at $(m, n+\frac{1}{2})$, similarly. Figure 1 shows the lattice positions of u, v and p involved in the equations for the temporal advancement of $u_{m+\frac{1}{2},n}$ and $v_{m,n+\frac{1}{2}}$, respectively. Finally, we replace (2.2), centred at (m, n), by

$$\delta_x u_{m-\frac{1}{2},n} + \delta_y v_{m,n-\frac{1}{2}} = 0. \tag{2.8}$$

The scheme (2.7) and (2.8) reduces numerical aliasing from that of a more natural, but less compact representation, where u, v and p are all defined at the same point (m, n). The above scheme also retains two exact integral conservation properties of the Navier–Stokes equations. For simple (e.g. periodic) boundary conditions, it follows that

$$\partial_t \sum_{m,n} u_{m+\frac{1}{2},n} = \partial_t \sum_{m,n} v_{m,n+\frac{1}{2}} = 0, \tag{2.9}$$

(conservation of momentum) and

$$\partial_t \sum_{m,n} (u^2_{m+\frac{1}{2},n} + v^2_{m,n+\frac{1}{2}}) = -\nu \sum_{m,n} [(\delta_x u_{m+\frac{1}{2},n})^2 + (\delta_y u_{m+\frac{1}{2},n})^2 + (\delta_x v_{m,n+\frac{1}{2}})^2 + (\delta_y v_{m,n+\frac{1}{2}})^2] \tag{2.10}$$

(conservation of energy for $\nu = 0$). That is, over the domain D of N lattice points the mean square velocity or energy E,

$$E = \langle \mathbf{u}.\mathbf{u} \rangle = \frac{1}{N} \sum_{m,n} (u^2_{m+\frac{1}{2},n} + v^2_{m,n+\frac{1}{2}}), \tag{2.11}$$

is 'semi-conserved' by the scheme (2.7): the nonlinear, inertial forces in (2.7) do not contribute to the dissipation of E. This is a discrete analogue of the corresponding property for the exact Navier–Stokes equations (2.1).

We discretize time derivatives in (2.7) using a combination of schemes: a centred or 'leap-frog' time difference for convective terms and a DuFort–Frankel representation for viscous terms (Richtmyer & Morton 1967, p. 176). The latter guarantees numerical stability of the viscous terms. The *inviscid* finite difference equations are second-order accurate in Δx, Δy and Δt. We recognize that the DuFort–Frankel scheme is first-order accurate, but we have used it only when the viscosity coefficient is small (Reynolds number $R \geqslant 750$). The viscous terms in the equations smooth and only slightly perturb the amplitudes of the long-wavelength features of our solutions. This fact is the result of computer runs with $\nu \equiv 0$ and ν finite and leads us to the physical conclusion that the large-scale phenomena are inviscid.

We advance $\mathbf{u}$ in time as follows:

(i) We obtain an intermediate velocity field $\mathbf{u}^*$ from the time discretized version of (2.7), dropping the pressure term.

(ii) We compute a pressure p at time t from the five-point discretized version of Poisson's equation in two dimensions,

$$\delta_x(\delta_x p_{m-1,n}) + \delta_y(\delta_y p_{m,n-1}) = \beta(\delta_x u^*_{m-\frac{1}{2},n} + \delta_y v^*_{m,n-\frac{1}{2}}). \tag{2.12}$$

The factor,

$$\beta = \frac{1}{2\Delta t} + \nu\left(\frac{1}{\Delta x^2} + \frac{1}{\Delta y^2}\right), \tag{2.13}$$

arises from the DuFort–Frankel treatment of viscous terms in step (i). In the following, we restrict D to be a rectangular domain and impose periodic boundary conditions. This enables us to solve (2.12) *exactly* and quickly, using fast discrete Fourier transform techniques (Hockney 1965; Williams 1969). This part of the complete algorithm is essentially new and differs from those of others (Welch *et al.* 1966; Chorin 1968), who use *iterative* methods to solve (2.12). However, our method cannot presently deal with the complicated boundary conditions treated by Harlow & Welch (1965).

(iii) Finally, we compute $\mathbf{u}$ at time $(t+\Delta t)$ from

$$u_{m+\frac{1}{2},n} = u^*_{m+\frac{1}{2},n} - \frac{1}{\beta}\delta_x p_{m,n}, \tag{2.14}$$

and a similar expression for $v_{m,n+\frac{1}{2}}$.

From (2.12) and (2.14) the incompressibility condition (2.8) is identically satisfied for all positive times. The complete algorithm remains quite stable for Δt of the order $\min(\Delta x, \Delta y)/|\mathbf{u}|$ or less. In a future publication, we will discuss properties of this algorithm, particularly how solutions depend upon lattice size and Reynolds number.

Although the energy E is semi-conserved by the above scheme (with $\nu = 0$), the same is not true for higher-order invariants of the two-dimensional Navier–Stokes equations (2.1) and (2.2). Recall that if the vorticity ω is introduced,

$$\omega = -\partial_y u + \partial_x v = -\nabla^2\psi, \tag{2.15}$$

where ψ is the stream function ($u = \partial_y\psi$, $v = -\partial_x\psi$), then after taking the curl of (2.1) and applying (2.2) we obtain

$$\partial_t\omega + \mathbf{u}.\nabla\omega = \nu\nabla^2\omega. \tag{2.16}$$

Equation (2.16) shows that, if $\nu = 0$ and simple boundary conditions are chosen, then any functional of ω over a subdomain moving with the fluid is conserved. For the above difference scheme, the mean-square vorticity, or 'enstrophy',

$$\langle\omega^2\rangle = \frac{1}{N}\sum_{m,n}\omega^2_{m+\frac{1}{2},n+\frac{1}{2}} \tag{2.17}$$

is *not* semi-conserved, using the obvious finite difference definition of ω centred at cell corners $(m+\frac{1}{2}, n+\frac{1}{2})$

$$\omega_{m+\frac{1}{2},n+\frac{1}{2}} = -\delta_y u_{m+\frac{1}{2},n} + \delta_x v_{m,n+\frac{1}{2}}. \tag{2.18}$$

Variations of the enstrophy therefore provide a gross assessment of the quality of solutions in the inviscid case. (For example, see figure 13.)

2.2. *Initial conditions*

Two *linearly unstable* initial conditions were chosen to simulate nearly parallel shear flows: a Gaussian mean profile with a single excited eigenmode and a Bickely mean profile with five excited modes. That is, at $t = 0$,

$$\mathbf{u}(x, y, 0) = [U(y) + u^{(1)}(x, y, 0), \quad v^{(1)}(x, y, 0)], \tag{2.19}$$

where

$$\epsilon = \max |\mathbf{u}^{(1)}(x, y, 0)| / \max |U(y)| \ll 1. \tag{2.20}$$

The experimental mean wake profile a short distance downstream of a thin flat plate is approximately

$$U(y) = U_0 - U_{c0} \exp(-y^2/\Delta^2) \tag{2.21}$$

(Sato & Kuriki 1961). The mean profile of a two-dimensional jet is approximately

$$U(y) = U_{c0} \operatorname{sech}^2(y/\Delta) \tag{2.22}$$

(Sato 1960). In our computations, we replace $U(y)$ by a profile $U^{(p)}(y)$, which is periodic with respect to a finite lateral interval L_y satisfying

$$L_y \gg 2\Delta; \tag{2.23}$$

and we restrict

$$-L_y/2 \leqslant y \leqslant L_y/2. \tag{2.24}$$

Specifically,

$$U^{(p)}(y) = \sum_{m=-\infty}^{m=+\infty} U(y + mL_y), \tag{2.25}$$

which is very close to $U(y)$ in $-L_y/2 \leqslant y \leqslant L_y/2$, provided (2.24) holds.

The perturbing velocity $\mathbf{u}^{(1)}$ is periodic in x, and is composed of symmetric eigenfunctions corresponding to *unstable* wave-numbers κ of the Rayleigh equation (Drazin & Howard 1966).

$$\left[\left(\frac{U^{(p)}}{U_0} - c\right)\left(\frac{d^2}{dy^2} - \kappa^2\right) - \frac{d^2}{dy^2}\left(\frac{U^{(p)}}{U_0}\right)\right]\phi = 0, \tag{2.26}$$

$$\phi(0) = 1, \quad \phi'(0) = \phi'(L_y/2) = 0.$$

Here ϕ is related to $\mathbf{u}^{(1)}$ through

$$\mathbf{u}^{(1)} = (\partial_y \psi^{(1)}, \ -\partial_x \psi^{(1)}), \tag{2.27}$$

$$\psi^{(1)} = \operatorname{Re}\{\phi(y) \exp[i(\kappa(x - ct) + \theta)]\}. \tag{2.28}$$

The eigenfunction boundary conditions in (2.26) are appropriate for periodic $\phi(y)$ symmetric about $y = 0$. Equation (2.26) is obtained by inserting (2.19) into (2.1) and retaining terms of order ϵ. Here θ is an arbitrary constant phase shift, and κ is the longitudinal or 'downstream' wave-number. The constant $c = c_r + ic_i$ is the complex phase velocity corresponding to wave-number κ. The unstable disturbances have growth rates $\kappa c_i > 0$. We make no use of the antisymmetric eigenfunctions of (2.26); for given κ, they have smaller growth rates than the corresponding symmetric eigenfunctions (Drazin & Howard 1966).

2.3. *Boundary conditions*

Figure 2 schematizes the flat-plate wake experiment, and helps us justify periodic boundary conditions on $0 \leqslant x \leqslant L_x$, $-L_y/2 \leqslant y \leqslant L_y/2$ as relevant to the experiment. A quantity (element) of fluid encompassing two low-pressure features leaves the end of the plate, undergoes a slight adjustment, and assumes a mean longitudinal velocity profile, as shown in the first box in the lower half of the figure. This unstable mean profile spreads as it moves downstream and develops into vortex pairs, shown in the second box.

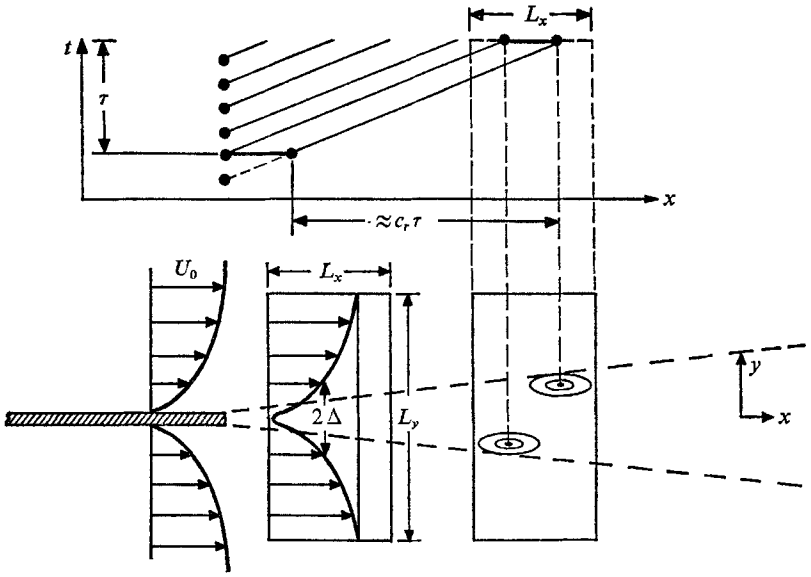

FIGURE 2. Schematic of two-dimensional flat plate wake and trajectories of primary vortex pairs in (x, t) space.

In order to describe accurately the development of small-scale structures, given the size and speed limitations of present-day computers, we cannot represent true downstream distance behind the plate by a spatial co-ordinate (cf. Fromm & Harlow 1963). To compare our results with experiment, we make a Taylor-like hypothesis (frozen flow), relating downstream distance to the computation time t. This correspondence is indicated schematically in the upper half of figure 2. Subsequent fluid elements originate at different times and traverse nearly parallel paths in (x, t) space.

Periodicity in the cross-stream direction is a reasonable approximation whenever condition (2.23) is satisfied, since the flow is observed *a posteriori* to remain laterally confined. If (2.23) is not satisfied, periodicity in the y direction is more appropriate to a description of the wake behind a uniformly spaced array of flat plates.

By imposing downstream periodic boundary conditions on a fluid element of

length L_x, we set a lower bound on the smallest wave-number (largest scale) which can develop. It is clear that we must take at least

$$L_x \geqslant 2\pi/\kappa_{\max}, \tag{2.29}$$

where $\kappa_{\max}$ is the most unstable wave-number according to linear theory. Physical systems which tend to develop subharmonics, such as a separated shear layer (Browand 1966), require that L_x be at least a factor of two larger than (2.29). Quite generally, energy in two-dimensional, incompressible fluids tends to flow into the lowest modes available (Batchelor 1953, p. 186; Fjortoft 1953). This phenomenon will be seen in § 4, in connexion with the evolution of a Bickely profile perturbed with five unstable modes. We therefore expect the experimentally observed L_x to increase slowly downstream, contrary to the assumptions of the present paper, where L_x is fixed. Moreover, Gaster (1968) and Mattingly (1968) have shown that experimental spatially amplified, and the present temporally amplified, disturbances cannot be accurately related by a linear transformation between time and space co-ordinates, using either the phase velocity c_r or the group velocity of the disturbance. For these and other reasons, complete quantitative agreement between our results and the experimental results of Sato & Kuriki should not be expected. In § 3, however, we find that the long time, fully nonlinear features of our calculations are in excellent qualitative agreement with experiment.

The longitudinal periodicity restricts the *temporal* (κ real) linear stability analysis to *discrete* modes,

$$\kappa = 2\pi k/L_x \quad (k = 1, 2, \ldots). \tag{2.30}$$

We shall refer to k as the mode number. The transverse periodic boundary conditions slightly modify the linear eigenvalues and eigenfunctions of (2.26), depending on the value of L_y. This effect is shown in figures 3(*a*) and 4(*a*) for the Gaussian and Bickely profiles, respectively. Here c_r and κc_i are, respectively, the phase velocities and growth rates of the symmetric eigenfunctions. Experimental c_r and κc_i from Sato & Kuriki (1961) are also shown in figure 3(*a*). The experimental phase velocities are in excellent agreement, whereas the experimental growth rates (filled circles) show about a 40 % deviation from the computed results.

2.4. *Computational modeling of experiment*

Figure 5 is a schematic showing the various choices made in performing a computation. The left side of the first line relates to the physical world, and the right to the numerical.

Given $U(y)$, we can specify only the arbitrary amplitudes ϵ and phases θ of the perturbing eigenfunctions. For given κ satisfying (2.29), we first compute symmetric eigenfunctions $\phi = \phi_r + i\phi_i$ and eigenvalues c from (2.24), according to the two-point boundary-value problem (2.26) (see appendix, §(i)). Figure 3 gives results for the Gaussian wake profile with $L_y = 16$. Here the values $U_0 = 1$, $U_{c0} = 0{\cdot}692$ and $\Delta = 1{\cdot}2011$ coincide with those used by Sato & Kuriki (1961).

Figure 3 (*b*) shows a typical symmetric eigenfunction for $\kappa = 0{\cdot}75$ ($\kappa_{\max} = 0{\cdot}7893$). Results for the Bickely profile with $U_0 = 1$ and $\Delta = 1$ are shown in figure 4.

Table 1 gives detailed properties of the eigenfunctions used in subsequent calculations with (2.1) and (2.2). Note that Sato & Kuriki (1961) computed $c_r = 0{\cdot}692$ and $\kappa c_i = 0{\cdot}140$ for $\kappa = 0{\cdot}832$. The corresponding values 0·701 and

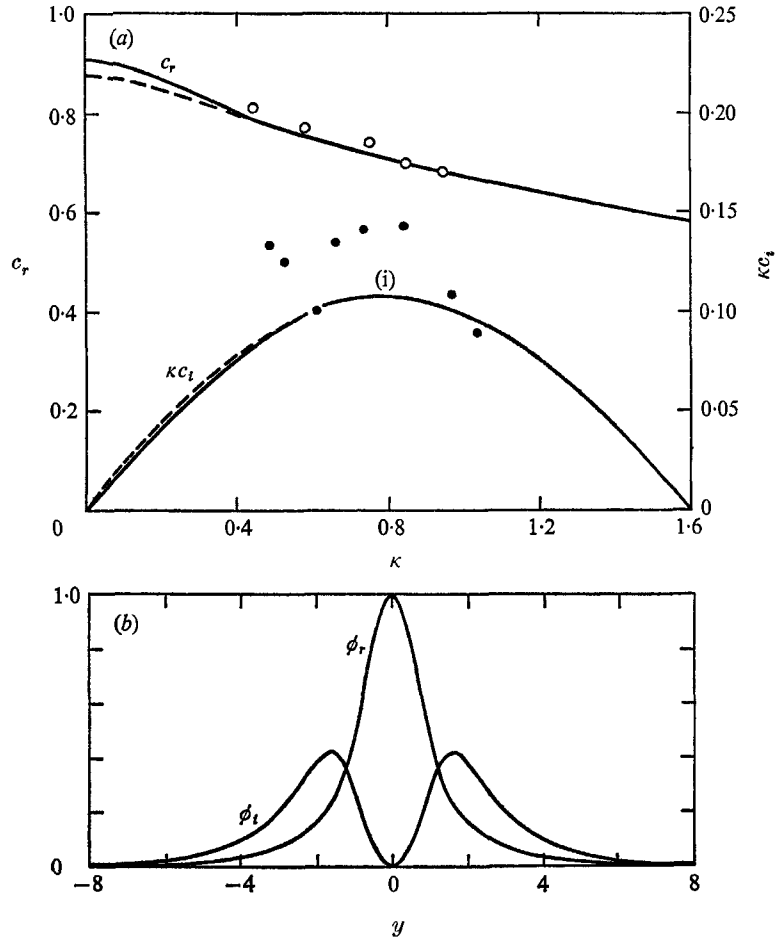

FIGURE 3. Linear eigenvalues and eigenfunctions for the y-periodic Gaussian profile: $U_0 = 1$; $U_{c0} = 0{\cdot}692$; $\Delta = 1{\cdot}2011$. (*a*) Linear dispersion relation (inviscid). ——, $L_y = 16$; – – –, 12. Sato & Kuriki: ○, c_r; ●, κc_i. (i) $\kappa = 0{\cdot}7893$, $c_r = 0{\cdot}7084$, $c_i = 0{\cdot}1363$. (*b*) Real and imaginary parts of the $\kappa = 0{\cdot}75$ symmetric eigenfunction $L_y = 16$. $c_r = 0{\cdot}7158$, $c_i = 0{\cdot}1430$.

0·107 from table 1 ($L_y = 12$) are invariant as $L_y \to \infty$. This discrepancy probably resulted because Sato & Kuriki applied their eigenfunction boundary conditions, which are appropriate for $L_y = \infty$, too near the flow centre.

Table 2 gives amplitudes ϵ, and phases θ, of velocity perturbations used in four calculations to be discussed below. In practice, we construct an initial perturbation stream function at cell corners $(m+\frac{1}{2}, n+\frac{1}{2})$ according to

$$\psi_{m+\frac{1}{2},n+\frac{1}{2}} = \sum_k \epsilon_k . \mathrm{Re}\{\phi_{n+\frac{1}{2}} \exp[i(2\pi k m N_x^{-1} + \theta_k)]\}, \tag{2.31}$$

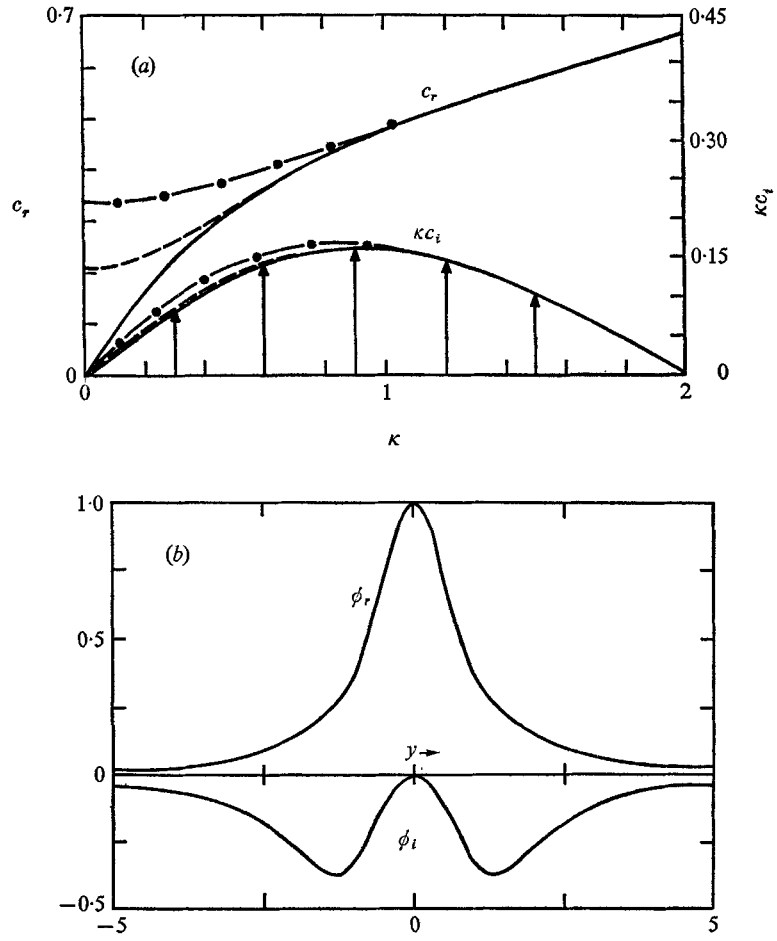

FIGURE 4. Linear eigenvalues and eigenfunctions for the y-periodic Bickely profile: $U_0 = 1$, $\Delta = 1$. (*a*) Linear dispersion relation (inviscid). ——, $L_y = \infty$; – – –, 10; —●—, 6. (*b*) Real and imaginary parts of the $\kappa = 0{\cdot}9$ symmetric eigenfunction $L_y = 10$. $c_r = 0{\cdot}4508$; $c_i = 0{\cdot}1789$.

Run	Profile	Mode no. k	κ	c_r	κc_i	Δ	L_x	L_y	$2\Delta/L_y$	U_0	U_{c0}
35	Gaussian	1	0·832	0·70058	0·10725	1·2011	7·5519	12·0	0·20	1·0	0·692
38	Gaussian	1	0·832	0·70058	0·10725	1·2011	7·5519	12·0	0·20	1·0	0·692
39	Gaussian	1	0·75	0·71576	0·10726	1·2011	8·3776	16·0	0·15	1·0	0·692
34	Bickely	1	0·3	0·25992	0·08589	1·0	20·944	10·0	0·20	0	1·0
		2	0·6	0·36423	0·14273	—	—	—	—	—	—
		3	0·9	0·45078	0·16101	—	—	—	—	—	—
		4	1·2	0·51944	0·14491	—	—	—	—	—	—
		5	1·5	0·57837	0·10274	—	—	—	—	—	—

TABLE 1. Growth rates (κc_i) and phase velocities (c_r) of symmetric eigenfunctions, y-periodic profiles

where $N_x = L_x/\Delta x$ and $N_y = L_y/\Delta x$ are even (the total number of lattice points $N = N_x N_y$ in (2.11) and (2.17)). The initial $\mathbf{u}^1$, defined on the staggered lattice of figure 1 by

$$u^{(1)}_{m+\frac{1}{2},n} = \delta_y \psi_{m+\frac{1}{2},n-\frac{1}{2}}, \quad v^{(1)}_{m,n+\frac{1}{2}} = -\delta_x \psi_{m-\frac{1}{2},n+\frac{1}{2}}, \tag{2.32}$$

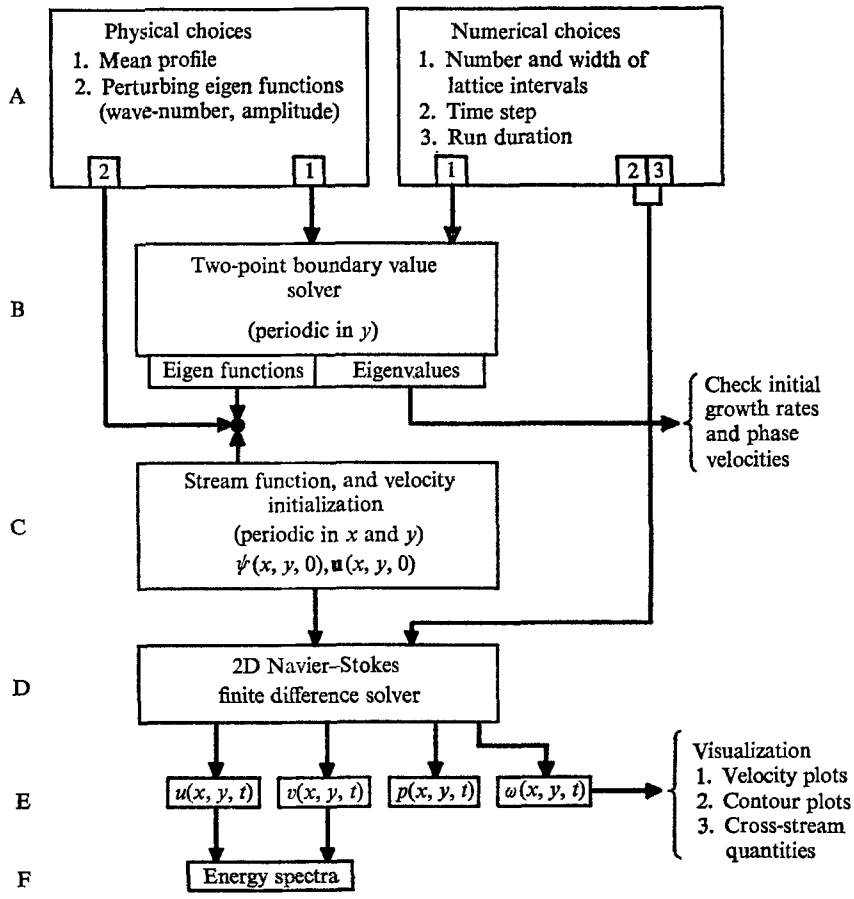

FIGURE 5. Flow chart for two-dimensional Navier–Stokes solver.

Run	Mode no. k	Exp. time t_E	Amplitude ϵ_k	Phase θ_k	Energy E_k	Mean defect flow energy E_0
35	1	9·3240	0·15	0	0·0012656	0·030036
38	1	9·3240	0·05	0	0·0001401	0·030036
39	1	9·3231	0·10	0	0·0003888	0·022527
34	1	11·643	0·069870	$3\pi/5$	0·0002000	0·066667
	2	7·0062	0·061494	$\pi/5$	0·0002000	—
	3	6·2108	0·054023	0	0·0002000	—
	4	6·9008	0·047985	$4\pi/5$	0·0002000	—
	5	9·7333	0·042980	$2\pi/5$	0·0002000	—

TABLE 2. Amplitudes, phases and energies of perturbed, symmetric eigenfunctions

satisfies (2.8) identically. The sum in (2.31) is extended over all initially excited mode numbers k with non-vanishing ϵ_k.

Table 2 also gives modal energies E_k of the initial velocity field *defect* $(u-U_0, v)$. We define *transverse* averages of the one-dimensional, *longitudinal* modal energies by

$$e_k = \frac{1}{N_y}\sum_n \left[\left|\frac{1}{N_x}\sum_m u_{m+\frac{1}{2},n}\exp(i2\pi km/N_x)\right|^2 + \left|\frac{1}{N_x}\sum_m v_{m,n+\frac{1}{2}}\exp(i2\pi km/N_x)\right|^2\right] \quad (2.33)$$

(cf. appendix, §(ii)). Then

$$E_0 = e_0 - U_0^2, \quad E_{N_x/2} = e_{N_x/2}, \quad (2.34)$$

and

$$E_k = 2e_k \quad (k = 1, \ldots, \tfrac{1}{2}N_x - 1). \quad (2.35)$$

The sum of the E_k gives the total energy E in the velocity field defect,

$$E = \sum_{k=0}^{\frac{1}{2}N_x} E_k. \quad (2.36)$$

Note that, since $E_k \ll E_0$ for $k > 1$ in the runs of table 2, the initial perturbation energies are small.

Run	No. perturbing modes	Lattice size $N_x \times N_y$	Δx	Δy	$\Delta/\Delta y$	Δt	Comp. cycles	Total exp. times t/t_E	R
35	1	128 × 128	0·05900	0·09375	12·8	0·05	1200	6·436	∞
38	1	64 × 64	0·11800	0·18750	6·4	0·05	1200	6·436	∞
39	1	128 × 128	0·06545	0·12500	9·6	0·05	2000	10·726	750·0
34	5	64 × 64	0·32725	0·15625	6·4	0·05	600	4·830	∞

TABLE 3. Run discretization parameters

Table 3 gives information concerning the spatial and temporal discretization for the various runs. The lattice interval Δx is determined from $\Delta x = L_x/N_x$ and Δy is chosen small with respect to Δ, the mean velocity lateral scale parameter (see table 3, column $\Delta/\Delta y$, which gives the number of lattice intervals in an initial lateral scale). The time step Δt in each run was chosen to be 0·05. A heuristic necessary condition for the *numerical* stability of the linearized version of (2.7), with perturbed shear profiles (2.19) and $\nu = 0$, is easily derived as

$$\Delta t \leqslant \Delta x/\max|U|. \quad (2.37)$$

For the present class of flows, condition (2.37) leads to stable results even after times when the flow has become highly nonlinear. Note, from table 3, that (2.37) is only marginally satisfied for runs 35 and 39.

2.5. *Flow visualization*

The results of our computations, namely $\mathbf{u}$ and p, are stored on magnetic tape and examined at selected time intervals, indicated in table 4. During the course of a computation we monitor the variation of global quantities. These include

energy, enstrophy and $\omega_{\max} - \omega_{\min}$, quantities conserved by the inviscid Navier–Stokes equations. Energy is semi-conserved by scheme (2.7), so that variations in E for $\nu = 0$ result from the time discretization and round-off errors.

At less frequent intervals, we 'visualize' the $\mathbf{u}$, p and ω fields, together with the downstream modal energies E_k. Experimental measurements, such as those given by Sato (1960) and Sato & Kuriki (1961), customarily refer to time-averaged

Run	Print interval in time steps	Available data in time steps	Experiment	Time steps = downstream interval (mm)	y = Cross-stream distance (mm)
35	40	20	Sato & Kuriki (1961)	100 = 5·7	1 = 1·14
38	100	20	Sato & Kuriki (1961)	100 = 5·7	1 = 1·14
39	50	25	Sato & Kuriki (1961)	100 = 5·7	1 = 1·14
34	20	20	Sato (1960)	100 = 12·3	1 = 2·40

TABLE 4. Available information and conversion to physical scales

properties measured by a stationary probe. We compare these with cross-stream profiles obtained by averaging variables over a full period in the downstream (x) direction:

(i) Mean longitudinal-velocity,

$$U(y,t) = \frac{1}{N_x} \sum_m u_{m+\frac{1}{2},n}. \tag{2.38}$$

(ii) Longitudinal-velocity fundamental and second harmonic amplitudes,

$$|u_k(y,t)| = \left| \frac{1}{N_x} \sum_m u_{m+\frac{1}{2},n} \exp(i2\pi km/N_x) \right| \quad (k = 1, 2), \tag{2.39}$$

where (2.39) is compared with Sato & Kuriki's $\overline{u_k^2}^{\frac{1}{2}}$.

(iii) Longitudinal-velocity phase,

$$\tan\theta_1(y,t) = -\sum_m u_{m+\frac{1}{2},n} \sin(2\pi m/N_x) / \sum_m u_{m+\frac{1}{2},n} \cos(2\pi m/N_x). \tag{2.40}$$

In the following, we also normalize the phase θ_1 to zero at the lower boundary,

$$\theta_1(-L_y/2, t) = 0, \tag{2.41}$$

in correspondence with the data of Sato & Kuriki (1961).

Data are displayed using a Stromberg Datagraphics 4060 electronic processor; examples are given below.

3. Evolution of a perturbed Gaussian profile (wake)

Runs 35, 38 and 39 of table 3 were made using the initial Gaussian profile (2.21). In each case, the initial perturbation mode number is approximately the most unstable according to linear theory. The parameters U_0, U_{c0} and Δ correspond to

those measured by Sato & Kuriki at $X = 30\,\text{mm}$ downstream of a thin, 30 cm long, polished aluminium airfoil in a wind tunnel with a free-stream velocity of $U_0 = 10\,\text{m sec}^{-1}$. The variables $\mathbf{u}$, x, y, t, etc., are non-dimensionalized with U_0 and b, the measured wake half-width at $X = 30\,\text{mm}$ ($b = 1{\cdot}14\,\text{mm}$). The Reynolds number R of run 39 (table 3) corresponds to the experimental,

$$R = (bU_0)/\nu = 750. \tag{3.1}$$

The corresponding R based on the airfoil length, in place of b, is 2×10^5. The last two columns of table 4 give the comparison between dimensionless and experimental time and length scales. Taylor's transformation, relating time intervals to downstream displacements of X, becomes

$$X_2 - X_1 = U_0 . (T_2 - T_1) = b . (t_2 - t_1), \tag{3.2}$$

where $(T_2 - T_1)$ is the dimensional time interval.

Runs 35 and 38 are similar except for changes in the lattice size and the level of the initial perturbation, and the results obtained for each are similar. In addition to a finite R, run 39 uses a larger L_y and a slightly smaller wave-number κ for the initial perturbation. Note, however, that the linear exponentiation time $t_E = (\kappa c_i)^{-1}$ is approximately constant among these runs.

3.1. *Velocity, pressure and vorticity fields*

Figures 6–8 show the evolution of $\mathbf{u}$, p and ω for run 39. Figure 6 gives the initial and final wake *defect* velocity fields plotted at one-fourth the total number of lattice points. Line segments emanating from dots give the magnitude and sense of the velocity at the segment centres. The superposed heavy lines were added to the machine plots to bring out salient features. At $t = 0$, the wake occupies 15 % of the computational lattice; the sinusoidal perturbation $\mathbf{u}^{(1)}$ is only barely evident. At $t = 100$ (2000 computation steps), the flow has evolved into a doubly periodic array of 'elliptical' vortices. Note that the flow remains confined to the central region. At late times, a 'secondary' pair of weak vortices appear near the upper and lower flow boundaries. For $t \geqslant 40$, the vortices translate to the right at about one longitudinal period per 10 time units.

Figure 7 gives the corresponding constant pressure contours (the vertical array of ellipses at the right will be discussed in § 3.3). The nine pressure levels shown are equally spaced between the high (H) and low (L) values of p. At $t = 100$, the high-pressure regions have become comparatively flat plateaus, in which the primary vortex low-pressure regions are embedded.

Figure 8 shows the evolution of lines of constant vorticity (2.18) for run 39. Nine levels are drawn in each figure between the positive or high (H) and negative or low (L) vorticity points. From $t = 20$–60, the vortex lines stretch to form long filamentary regions. This feature is more evident in the inviscid run 35, and is consistent with the $\nu = 0$ vorticity equation (2.16), which conserves area between lines $\omega =$ constant. The fragmented structure at $t = 40$ represents the break-up of narrowing filaments due to the lack of spatial resolution. This structure is more strongly evident in the inviscid runs 35 and 38; and, for these runs, the consequent loss of information probably results in numerical irreversibility.

For $t = 60$–100, the effect of viscosity is evident in figure 8: the vortices separate from one another, thus altering the original topological structure at $t = 0$. Note the appearance of the more rapidly moving secondary vortices at $t = 100$

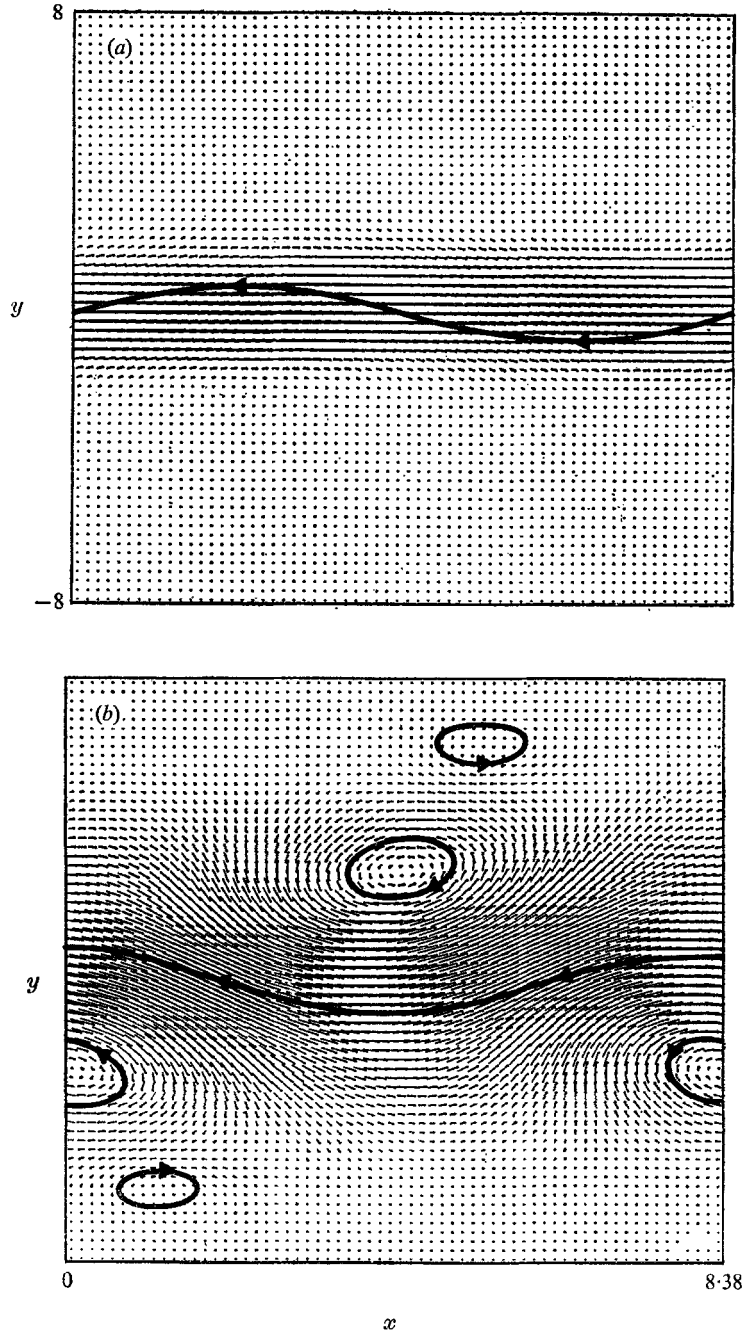

FIGURE 6. Velocity fields for a perturbed Gaussian profile (run 39) at times (*a*) $t = 0$, and (*b*) 100. The free-stream velocity U_0 has been removed.

(cf. figure 6). A more detailed examination of the evolution of vorticity contours reveals that the secondary vortices originate in the interior of the flow, and are swept out and formed on the flow extremities. At $t = 40$, we see the first definite signs of secondary vortices.

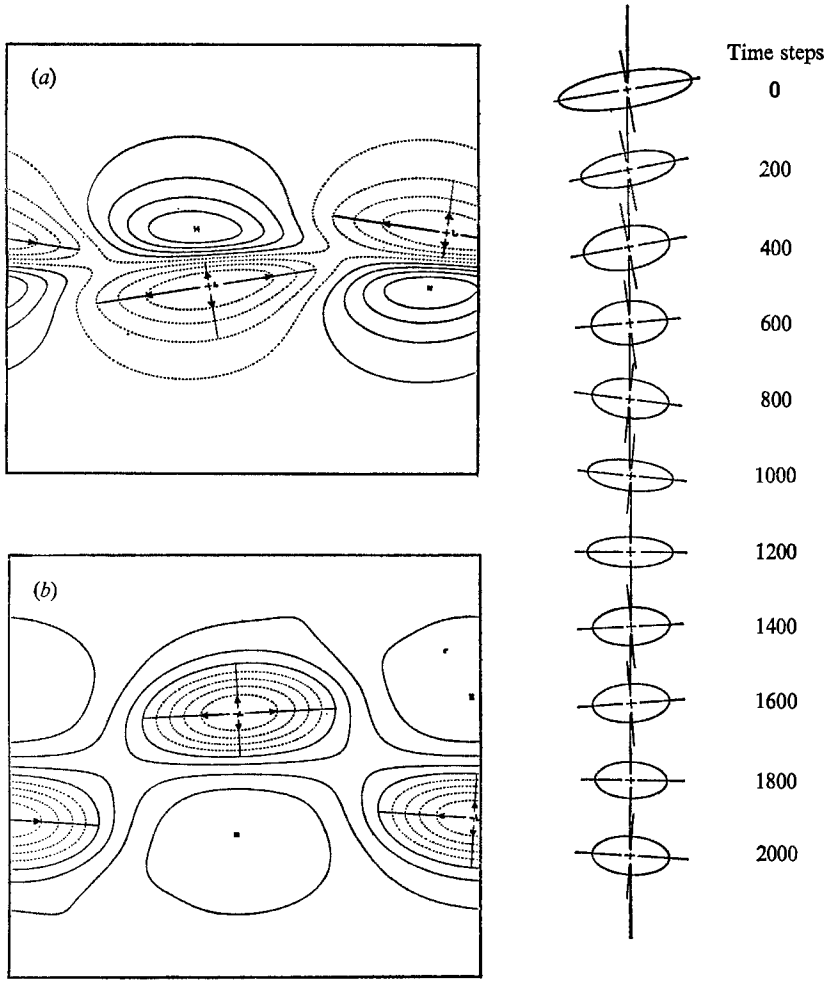

FIGURE 7. Constant pressure contours (9 levels, 8 contour lines) for a perturbed Gaussian profile (run 39) at (*a*) $t = 0$, and (*b*) 100 (one-mode Gaussian wake). The vertical array of ellipses shows the contour pattern surrounding the low pressure point in the lower half of the flow at intervals of 200 computation steps. The horizontal and vertical scales are the same as in figure 8. Note that they differ in such a way that the ellipses appear more elongated and have smaller inclination angles than in actuality. (See figure 11 (*c*).)

3.2. *Mean cross-stream features and comparison with experiment*

The first two columns of figure 9 show cross-stream distributions of the mean flow properties (2.38)–(2.40). The first column shows the short-time evolution from $t = 0$ to 12·5 ($0 \leqslant t/t_E \leqslant 1{\cdot}34$). At the latter time, the mean flow $U(y, t)$ approximately agrees with measured data from Sato & Kuriki (1961) at

$X = 40$ mm (open circles in column one). Over these times, the downstream velocity fundamental grows exponentially, in agreement with linear theory, as shown in column one of figure 9(*b*). Experimental points for $|u_1|$ and $|u_2|$ (on arbitrary vertical scales, not specified by Sato & Kuriki) are also shown in figures 9(*b*) and 9(*c*). The main features of each are in agreement with the computed results. The initial development of the fundamental phase θ_1 is shown in figure 9(*d*).

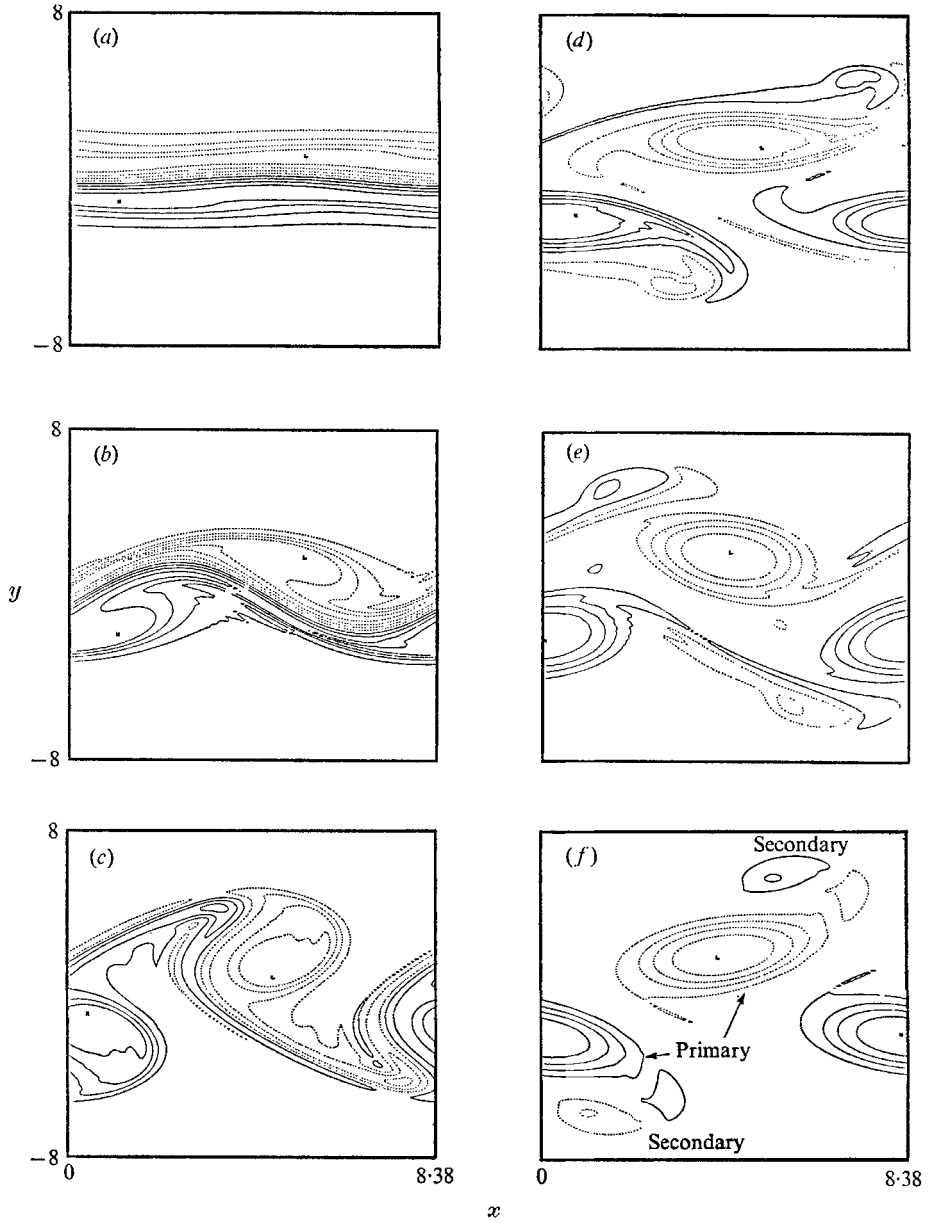

FIGURE 8. Constant vorticity contours (9 levels) for a perturbed Gaussian profile (run 39) at times (*a*) $t = 0$, (*b*) 20, (*c*) 40, (*d*) 60, (*e*) 80, (*f*) 100.

For times larger than t_E, the flow evolution becomes fully nonlinear. Computed results at selected times $t = 35$, 62·5 and 87·5 are shown in the second column of figure 9. The mean flow $U(y,t)$ spreads to approximately twice its initial width and rises to a maximum central value $U_c = U(0,t) = 0{\cdot}683$ at $t = 31$.

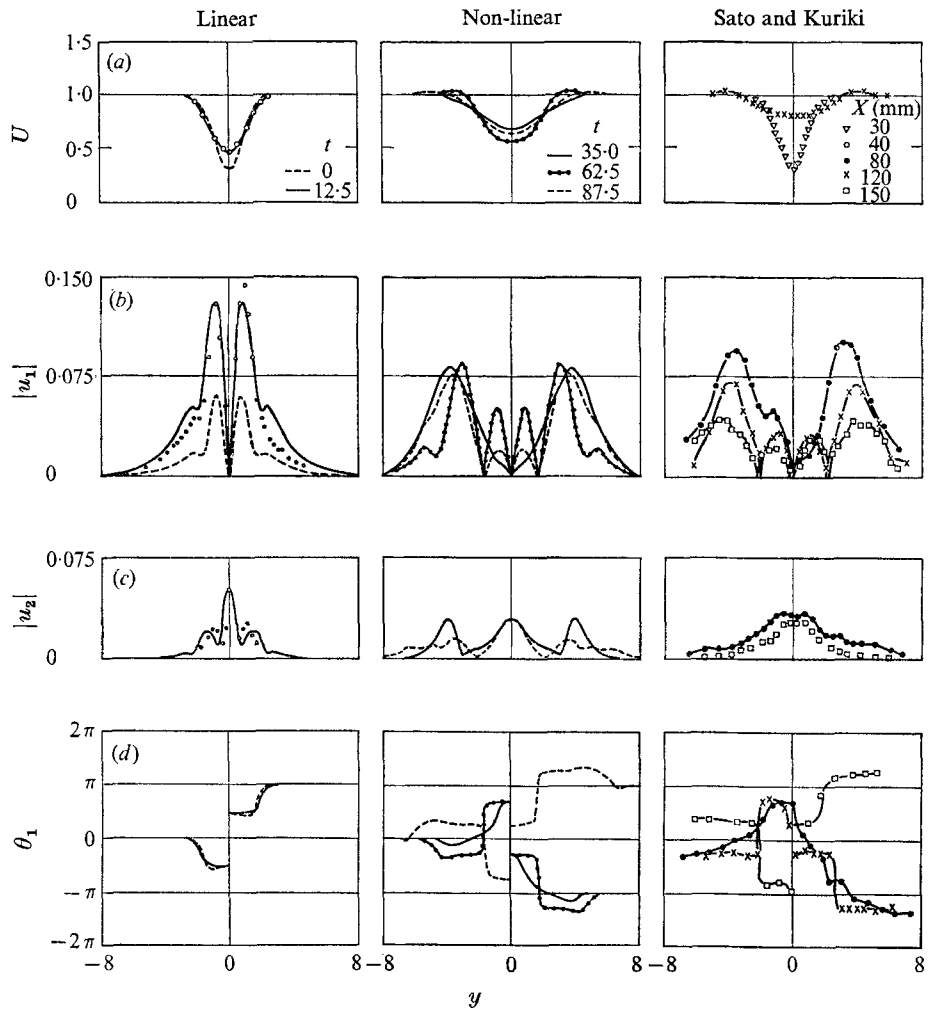

FIGURE 9. Downstream averaged cross-stream features for the Gaussian wake (run 39), and experimental data from Sato & Kuriki. (*a*) Mean longitudinal velocity profile. (*b*) Amplitude profile of longitudinal velocity fundamental. (*c*) Amplitude profile of longitudinal velocity second harmonic. (*d*) Phase profile of longitudinal velocity fundamental. Compare values of t in (*a*) linear, nonlinear with values of X in (*a*) Sato & Kuriki.

This compares with the experimental maximum of $U_c = 0{\cdot}84$ (Sato & Kuriki 1961, figure 28). Thus, although the curves resemble one another they disagree in magnitude. This small discrepancy is probably due to our restriction on the largest scale available to the flow for longitudinal evolution. That is, if we had a consistent method for allowing L_x to increase (possibly associating it with

estimated or experimental information on the evolution of longitudinal gradients), then the flow would spread downstream, and U_c would increase. U_c then *decreases*; and, at $t = 44$, U develops an 'overshoot' at the outer edges of the wake. The latter is an observed property of the Sato & Kuriki experiment (1961, figures 2, 22),

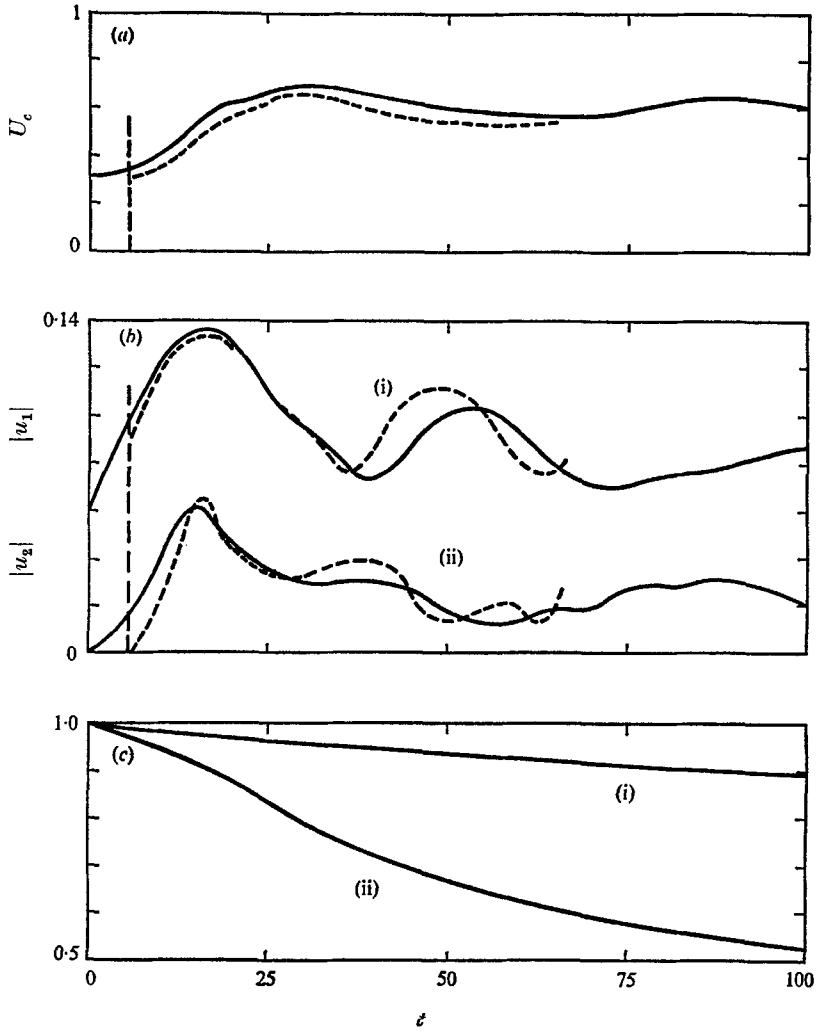

FIGURE 10. Evolution of mean features for the Gaussian wake (runs 35, 39). Run 35 has a stronger initial perturbation; its time scale has been shifted for clarity by 6 units. ——, $R = 750$; – – –, ∞. (*a*) Centre line mean longitudinal velocity. (*b*) Longitudinal velocity fundamental (maximum amplitude) (i), and second harmonic (centre line amplitude) (ii), (*c*) Energy and mean square vorticity: (i) $E/E_{t=0}$; (ii) $\langle\omega^2\rangle/\langle\omega^2\rangle_{t=0}$.

shown in the third column of figure 9(*a*). This phenomenon is simply the result of primary vortex circulation at the lateral flow extremities, seen in figure 6(*b*). The overshoot reaches a maximum of $U = 1{\cdot}039$ at $t = 61$, and shortly afterwards U again begins to increase. The complete time evolution of U_c for run 39 is shown in figure 10(*a*).

The corresponding nonlinear development of $|u_1(y,t)|$ is shown in figure 9(*b*). The experimental data in column three has the same vertical normalization as that in column one. The experimental data at $X_1 = 120$ and $X_2 = 150$ mm show off-axis nulls at $y = \pm 2$, as do the computed results at times $t_1 = 62{\cdot}5$ and $t_2 = 87{\cdot}5$. The corresponding relation between X and t is in good agreement with the Taylor transform (3.2). The computational results show, moreover, that these nulls in $|u_1|$ are a nearly periodic occurrence. We will return to a discussion of this long-time periodicity in § 3.3. As in the case with U, the experimental *amplitudes* of $|u_1|$ show quantitative differences from the computed results.

Columns two and three of figures 9(*c*) and 9(*d*) show similar comparisons between computed and experimental values of $|u_2(y,t)|$ and $\theta_1(y,t)$. The experimental $|u_2|$ are somewhat inaccurate, as stated by Sato & Kuriki. The comparison for θ_1 is quite good.

Figure 10 gives the time development of $U(0,t)$, $\max_y |u_1(y,t)|$ and $|u_2(0,t)|$, for run 39, and compares the results with those of the inviscid run 35. For clarity, the $t = 0$ ordinate of run 35 has been shifted to the right by 6 units, to compensate for an initially stronger velocity perturbation (table 2). Because of aliasing errors, we terminated this run sooner than the others. Note that the qualitative features of the results are unchanged: the main effects are inviscid.

Figure 10(*c*) gives the time evolution of E and $\langle\omega^2\rangle$ for run 39. Note that viscosity decreases the defect velocity energy by only 10% during this computation.

3.3. *A new temporal subharmonic frequency*

Figure 11 summarizes time-dependent properties of the constant pressure contours of run 39 (cf. figure 7). The vortex position and longitudinal velocity in figures 11(*b*), (*c*) are obtained by following the pressure lows (L) of the primary vortices. The initial motion of the vortices is governed by linear theory, as shown in figure 11(*c*). The linear wave-speed c_r indicated there is that of run 39 given in table 1.

After a short transition time, the primary vortices reach an approximate equilibrium configuration, centred at $y = \pm 1$ and moving with constant velocity $c_r = 0{\cdot}83$. Note from figure 11(*b*) that the non-dimensional wake half-width $b(t)$, defined from $U(b,t) = U(0,t)/2$, is approximately *twice* its initial value over these late times. This agrees with the data of Sato & Kuriki. The vortex separation ratio at $t = 100$ is

$$\text{(transverse distance/longitudinal distance)} = 0{\cdot}24, \tag{3.3}$$

where the distances are measured between low-pressure features.

We assert that many of the detailed properties observed in the computed and experimental results of figure 9 are explained by *a slow 'nutation' of the elliptical primary vortices with respect to the horizontal.* This effect is seen on the right of figure 7. Here, we isolate the contour lines surrounding the low-pressure point of the lower primary vortex, and focus attention on the angle of inclination to the horizontal made by the major axes of these contours. The time evolution of this

angle is indicated by the solid curve in figure 11(*a*). After the initial transition time, the vortex angle possesses a long-time quasi-periodicity with approximate frequency

$$f_N \simeq 0{\cdot}16U_0/L_x = 0{\cdot}030\kappa_{\max}c_r. \tag{3.4}$$

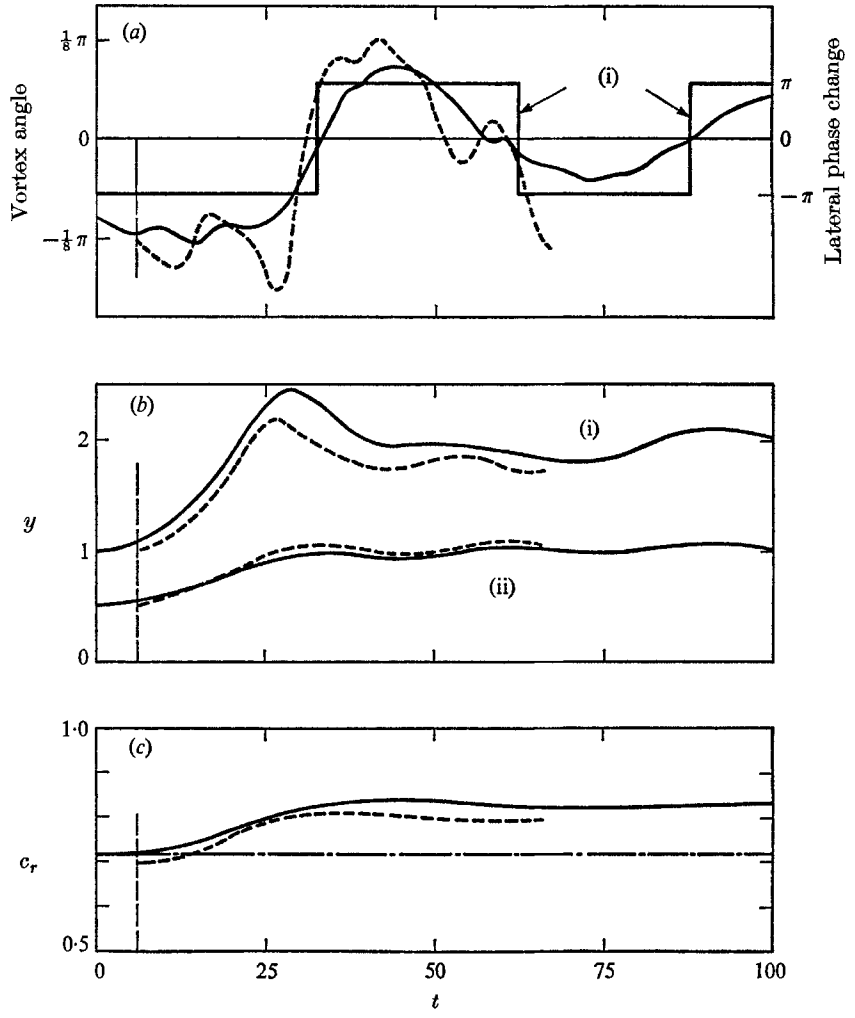

FIGURE 11. Temporal properties of the primary vortices for the Gaussian wake (runs 35, 39). ——, $R = 750$; – – –, ∞; —·—·—, linear wave speed. (*a*) Vortex inclination angle and velocity fundamental total lateral phase change (i). (*b*) Upper vortex transverse position (i), and wake half-width (ii). (*c*) Vortex longitudinal speed c_r compared with linear theory.

Here U_0 is the free-stream velocity at infinity, L_x is the longitudinal interval occupied by a primary vortex pair moving with velocity c_r, and $\kappa_{\max}$ is the linearly most unstable wave-number. The nutation frequency is only weakly dependent on viscosity, as seen from the superposed results of runs 35 and 39 in figure 11(*a*). The nutating ellipse is also evident in the vorticity contours of figure 8.

The solid, horizontal-vertical curve in figure 11 (*a*) gives the time evolution of the total lateral phase change,

$$\theta_1(-L_y/2, t) - \theta_1(L_y/2, t). \tag{3.5}$$

Note that (3.5) experiences an abrupt change of 2π whenever off axis nulls of $|u_1|$ appear in figure 9 (*b*). From figure 11 (*a*) we see that *phase reversal occurs whenever the elliptical primary vortex becomes aligned with the free-stream flow direction.*

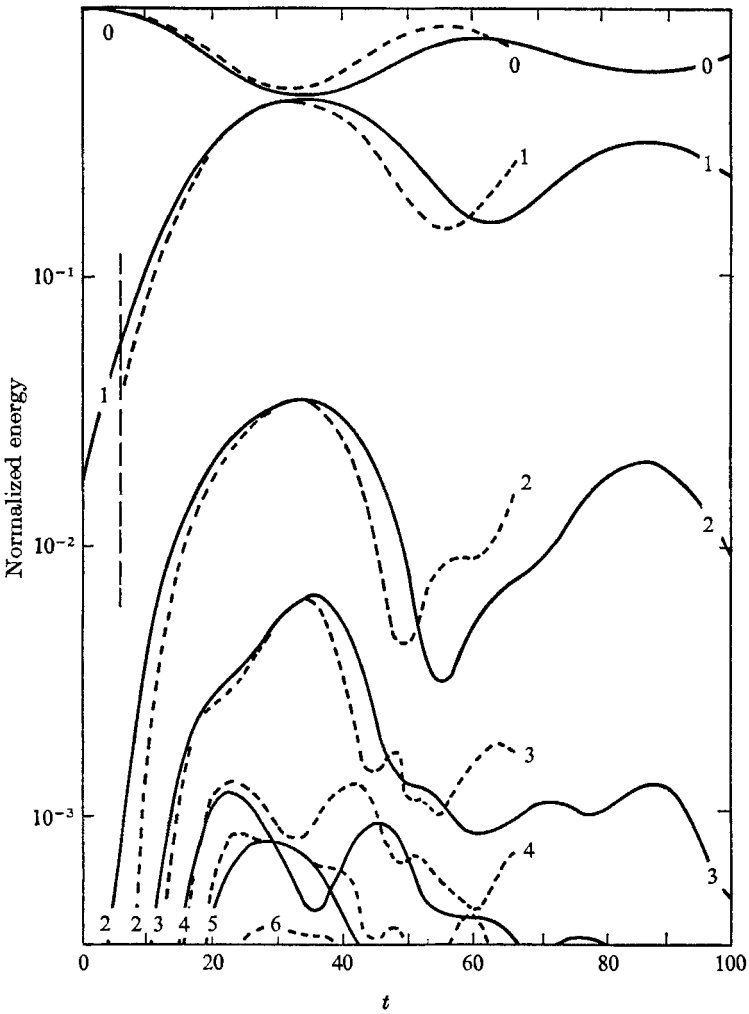

FIGURE 12. Downstream modal energy variations $E_k(t)/E(t)$ for the Gaussian wake (runs 35, 39). ——, $R = 750$; – – –, ∞.

3.4. *Large wave-number spectral properties*

Figure 12 gives the time evolution of the normalized modal energies E_k/E (equations (2.33)–(2.35)) plotted on a log scale, for runs 39 and 35, with the time axis shifted by 6 units as before. The curves are labelled according to mode number $k = 0, 1, \ldots$. It is evident that in both the viscous and inviscid cases the

energy in the first few harmonics shows a nearly periodic variation at the nutation frequency f_N.

This result demonstrates that indiscriminate application of Landau's conjecture (Landau 1944) can lead to false conclusions regarding asymptotic properties of solutions. Our results suggest that an expansion which retains three longitudinal modes ($k = 0$, 1 and 2) and two transverse modes ($k = 1$ and 2) should adequately describe the dynamics. However, in the corresponding first-order ordinary differential equations for complex mode amplitudes, one must allow for *self-consistent*, or time-varying coefficients (cf. Eckhaus 1965, chs. 2, 3, esp. (2.7.3)–(2.7.5)), since the mean flow and fundamental exchange energy in a nearly periodic manner after the linear growth régime.

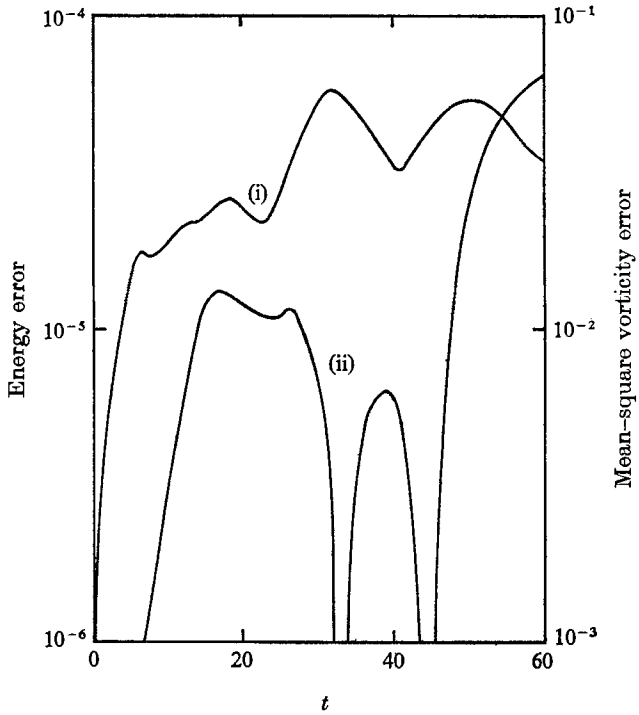

FIGURE 13. Energy and enstrophy variations for the inviscid Gaussian wake (run 35). (i) $(E/E_{t=0}) - 1$; (ii) $(\langle\omega^2\rangle/\langle\omega^2\rangle_{t=0}) - 1$.

Figure 12 also shows that even in the inviscid case, all but a fraction of a per cent of the total energy E resides in modes 0, 1 and 2. The numerical integrity of the inviscid run 35 is shown in figure 13. The variation of total energy $[(E/E_{t=0}) - 1]$ remains somewhat less than 10^{-4}; the variation of mean-square vorticity $[(\langle\omega^2\rangle/\langle\omega^2\rangle_{t=0}) - 1]$ remains of order of 1 %, except for the final portion of the calculation, where variations of order 7 % are observed. Note that $t = 0$ on this figure corresponds to $t = 6$ on figures 11 and 12.

Figure 14 shows the time variation of log–log plots of the downstream modal energy spectrum E_k versus $k + 1$. These results are relevant to the two-dimensional theories of homogeneous, isotropic turbulence; they are also a prediction of

spectra for high Reynolds number, incompressible wake experiments, as yet to be performed. Batchelor (1969) has argued on dimensional grounds that high Reynolds number, two-dimensional, homogeneous and isotropic flows should develop an inertial range of mode numbers k, for which

$$E_k \sim k^{-\mu} \quad (\mu = 3). \tag{3.6}$$

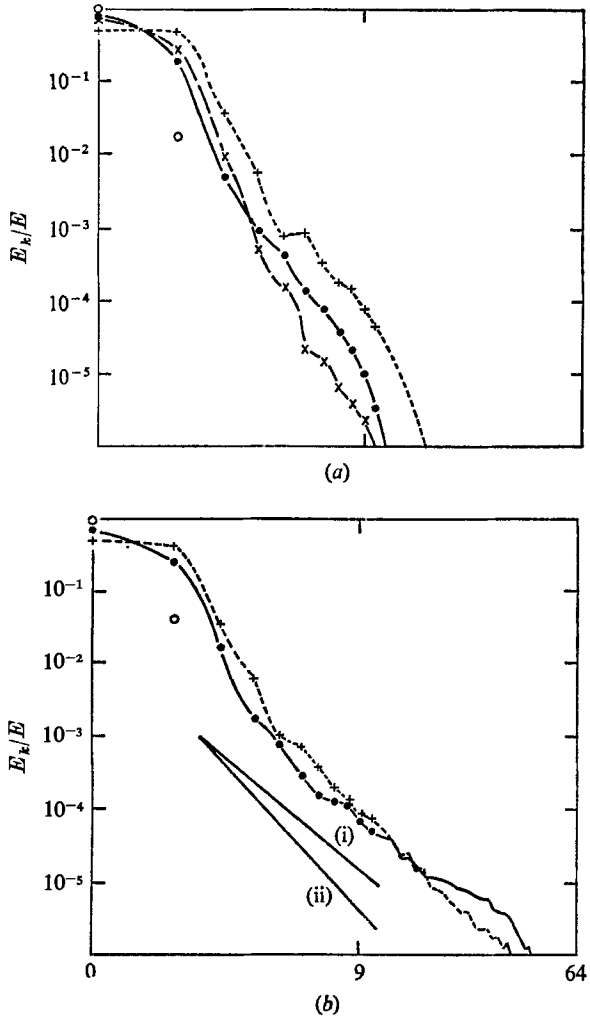

FIGURE 14. Downstream modal energy spectra for the Gaussian wake (runs 35, 39). ○, $t = 0$; +, 30; ●, 60; ×, 100. (*a*) $R = 750$, (*b*) ∞, ((i) $(k+1)^{-3}$, (ii) $(k+1)^{-4}$).

In the appendix, §(ii), we discuss the relation between $E_k(t)$ and the more commonly defined energy spectrum function $E(\kappa, t)$ from the continuum theory of two-dimensional isotropic turbulence (Batchelor 1969). If we assume that isotropy is a good approximation for large mode numbers after a few exponentiation times, then from figure 14(*a*) it is evident that $R = 750$ is still too small for (3.6) to hold. Figure 14(*b*) shows the corresponding evolution with $\nu = 0$ (run 35).

After about one exponentiation time t_E, modes larger than $k = 4$ develop a fairly stationary equilibrium spectrum of the form (3.6), where $3 < \mu < 4$. Note that, to the final time shown, $t = 60$ (6·44 exponentiation times), the largest mode numbers begin to show the effects of cumulative numerical aliasing. That is, the *apparent* k^{-3} spectrum at mid-range wave-numbers in figure 14(*b*), $t = 100$ is due to the 'unphysical' feedback of energy from the high-to-low end of the spectrum.

These results are to be compared with the numerical computations of Lilly (1969). He studied a driven viscous fluid in two dimensions on a coarser lattice (64 × 64 compared to our 128 × 128). He observed a spectrum, approximately k^{-3}. Our spectrum falls off more rapidly, that is μ is closer to 4.

4. Development of subharmonics in the evolution of a Bickely profile

In § 2 we noted that the downstream periodic boundary conditions limit the smallest wave-number that can develop in the flow. In runs 35, 38 and 39, relation (2.29) was only marginally satisfied, so that subharmonics of $\kappa_{\max}$ do not

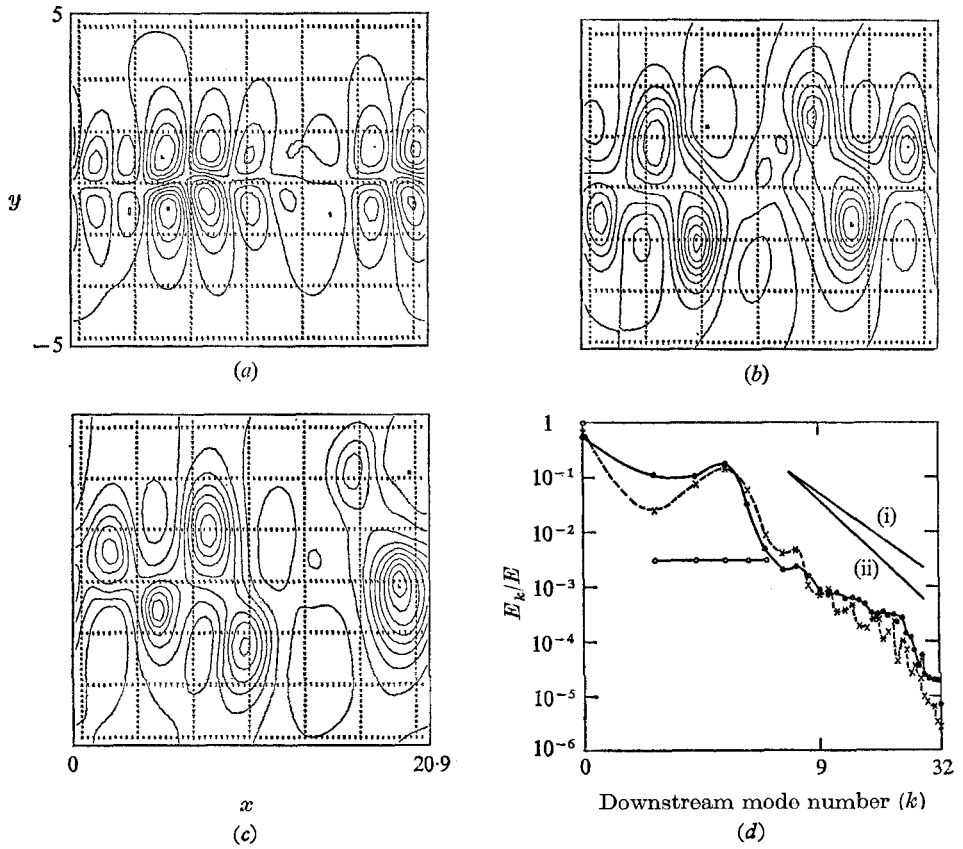

FIGURE 15. Five-mode-perturbed Bickely profile (run 34). (*a*) Pressure contours, $t = 0$; (*b*) 18; (*c*) 30; (*d*) Downstream modal energy spectra. ○, $t = 0$; ×, 18; ●, 30. (i) $(k+1)^{-3}$; (ii) $(k+1)^{-4}$. Mode 3 is the most unstable.

exist. In § 4 we study effects of the presence of subharmonics on the long-time flow development.

Run 34 of table 3 was made using the Bickely 'jet' profile (2.22) perturbed with five unstable modes, as indicated in figure 4(*a*). In addition to the central, most unstable mode $\kappa_{\max} = 0{\cdot}9$, we perturb subharmonics $\kappa = 0{\cdot}3$ and $0{\cdot}6$, together with harmonics $\kappa = 1{\cdot}2$ and $1{\cdot}5$. The perturbing modes were equally excited at $t = 0$, where from table 2, $E_k/E = 0{\cdot}00296$, $k = 1, \ldots, 5$. The Reynolds number was infinite.

Figure 15 summarizes the flow development up to a time $t/t_E = 4{\cdot}83$, where t_E is the linear exponentiation time of the fastest growing mode ($k = 3$). The constant pressure contours between figures 15(*a*) and (*c*) reveal an effect absent in previous sections, namely, the gradual merging of smaller into larger vortices. This effect is seen more clearly in figure 15(*d*), which gives the corresponding development of the modal energies. At $t = 0$, the five equally excited modes together with the mean, or $k = 0$ mode are indicated by open circles. At $t = 18$ the $k = 3$ (most unstable) mode dominates the remaining modes $k > 0$, as one would expect from linear theory. However, by $t = 30$ we note a large increase in the energy content of the $k = 1$ subharmonic, as a result of the gradual merging of smaller vortices (Batchelor 1953).

Figure 15(*d*) again shows that the higher harmonics for inviscid flows evolve into an approximate equilibrium of the form (3.6), $3 < \mu < 4$.

5. Conclusions

Direct numerical integration of the incompressible Navier–Stokes equations provides at present the most reliable means for studying the evolution of two-dimensional shear flows. It also provides a means for evaluating analytical hypotheses about these flows made in the past. In the present work we have used a very high resolution lattice (128×128 points) to study the dynamical evolution of a perturbed Gaussian wake. Except for very short times, essentially those where linear theory is valid, we find no support for the usual boundary-layer approximation, that the ratio of longitudinal to transverse flow derivatives should remain small, according to

$$\partial_x/\partial_y = O(R^{-\frac{1}{2}}) \ll 1 \tag{5.1}$$

(Ko, Kubota & Less 1970). This is due to the formation of elliptical vortex pairs, whose origin is basically an inviscid phenomenon. After approximately two exponentiation times of the linearly most unstable mode, the flow evolves in a quasi-periodic manner, seen as a slow nutation of elliptical vortices with respect to the downstream direction and undoubtedly the result of an interaction between the mean flow and the vortex states. This subharmonic frequency should be sought experimentally, and elucidated theoretically. The numerical results indicate that viscosity and downstream harmonics higher than the second play a negligible role in this phenomenon. For zero viscosity we also predict, after moderate times, that the energy spectrum behaves as $k^{-\mu}$, where $3 < \mu < 4$. A more precise value of μ can be determined by studies with more refined meshes.

The authors gratefully acknowledge conversations with Professor C. H. Su and programming assistance by L. K. Russell and L. B. Dozier. Parts of this paper were presented at: Symposium on Turbulence, Boeing Scientific Research Laboratories, 23–27 June 1969; Symposium on Computational Physics, UKAEA, Culham Laboratory, 28–31 July 1969; and Symposium on Instability of Continuous Systems, IUTAM, Herrnalb, 8–12 September 1969.

Appendix

(i) *Solution of the eigenvalue problem* (2.26)

The solution of (2.26) for symmetric eigenfunctions of periodic mean profiles (2.25) is accomplished using a search procedure for the eigenvalue c. For given κ, c is assumed to lie in a given (sufficiently large) square $R^{(0)}$ in the complex c plane. The one-point boundary-value problem for (2.26) with

$$\phi(0) = 1, \quad \phi'(0) = 0 \tag{A 1}$$

is then solved successively on a uniformly spaced lattice of c values subdividing $R^{(0)}$ (usually 10×10 intervals). A fourth-order predictor-corrector scheme with relative accuracy 10^{-5} was used for the results of § 2.2. The lattice value of c which minimizes $|\phi'(L_y/2)|$ provides a first guess $c^{(1)}$ for the eigenvalue c. The above procedure is then repeated on a smaller square $R^{(1)}$ surrounding $c^{(1)}$, and this search is refined until the sequence $c^{(n)}$ converges with relative accuracy 10^{-5}. Antisymmetric eigenfunctions can be similarly computed from the two-point boundary-value problem (2.26) with

$$\phi'(0) = 1, \quad \phi(0) = \phi(L_y/2) = 0. \tag{A 2}$$

(ii) *The relation between E_k and the energy spectrum function of continuum turbulence theory*

The discrete *longitudinal* modal energies e_k (2.33) are related to the energy spectrum $E(\kappa)$ in the theory of two-dimensional, homogeneous and isotropic turbulence (Batchelor 1969). Assume that $\mathbf{u}(x, y)$ is a spatially homogeneous and isotropic velocity field defined everywhere in (x, y) space. We can regard e_k as a discrete analogue to

$$S(\kappa) = \frac{1}{\pi} \int_{-\infty}^{\infty} \langle \mathbf{u}(x, y) . \mathbf{u}(x+r, y) \rangle . \cos \kappa r \, dr. \tag{A 3}$$

Here, κ denotes a continuous, scalar wave-number. The quantity in brackets depends only on r, using the spatial homogeneity of $\mathbf{u}$. We have normalized S in a manner analogous to (2.36)

$$\int_0^{\infty} S(\kappa) \, d\kappa = \langle \mathbf{u} . \mathbf{u} \rangle. \tag{A 4}$$

The two-dimensional energy spectrum function E can be defined from

$$\langle \mathbf{u}(x, y) . \mathbf{u}(x+r, y) \rangle = \int_{-\infty}^{\infty} E(\kappa) J_0(\kappa r) \, d\kappa, \tag{A 5}$$

where J_0 is the zeroth-order Bessel function. The relation between E and S follows after substituting (A 5) into (A 3):

$$S(\kappa) = \frac{4}{\pi}\int_0^\infty \frac{E[(\kappa^2+\lambda^2)^{\frac{1}{2}}]}{(\kappa^2+\lambda^2)^{\frac{1}{2}}}\,d\lambda. \tag{A 6}$$

Relation (A 6) shows that, if $E(\kappa)$ is a power law

$$E(\kappa) \sim \kappa^{-\mu} \quad (\mu > 0), \tag{A 7}$$

then $S(\kappa)$ retains the same power law form.

REFERENCES

Batchelor, G. K. 1953 *Homogeneous Turbulence.* Cambridge University Press.

Batchelor, G. K. 1969 *Phys. Fluids Suppl.* II, **12**, 233.

Browand, F. K. 1966 *J. Fluid Mech.* **26**, 281.

Chorin, A. J. 1968 *Math. Comput.* **22**, 745.

Drazin, P. G. & Howard, L. N. 1966 *Adv. Appl. Mech.* **9**, 1.

Eckhaus, W. 1965 *Studies in Non-linear Stability Theory.* Springer.

Fjortoft, R. 1953 *Tellus*, **5**, 225.

Fromm, J. E. & Harlow, F. H. 1963 *Phys. Fluids*, **6**, 975.

Gaster, M. 1968 *Phys. Fluids*, **11**, 723.

Harlow, F. H. & Welch, J. E. 1965 *Phys. Fluids*, **8**, 2182.

Hockney, R. W. 1965 *J. Comp. Mach.* **12**, 95.

Ko, D. R., Kubota, T. & Lees, L. 1970 *J. Fluid Mech.* **40**, 315.

Landau, L. D. 1944 *C.R. Acad. Sci. U.R.S.S.* **44**, 311.

Landau, L. D. & Lifschitz, E. M. 1959 *Fluid Mechanics.* Pergamon.

Lilly, D. K. 1969 *Phys. Fluids Suppl.* II, **12**, 240.

Mattingly, G. E. 1968 *Princeton University, Dept. of Aerospace and Mech. Sci., Rep.* 858.

Richtmyer, R. D. & Morton, K. W. 1967 *Difference Methods for Initial-Value Problems.* Interscience.

Sato, H. 1960 *J. Fluid Mech.* **7**, 53.

Sato, H. & Kuriki, K. 1961 *J. Fluid Mech.* **11**, 321.

Welch, J. E., Harlow, F. H., Shannon, J. P. & Daly, B. J. 1966 *Los Alamos Sci. Lab. Rep.* LA-3425.

Williams, G. P. 1969 *J. Fluid Mech.* **37**, 727.

Zabusky, N. J. 1966 *Non-linear Partial Differential Equations* (ed. W. Ames). Academic.